SCIENTIFIC REPORTS

OPEN

Conduction-band effective mass and bandgap of $ZnSnN_2$ earth-abundant solar absorber

Received: 21 July 2017
Accepted: 17 October 2017
Published online: 08 November 2017

Xiang Cao[1], Fumio Kawamura[2], Yoshihiko Ninomiya[1], Takashi Taniguchi[2] & Naoomi Yamada[1]

Pseudo III-V nitride $ZnSnN_2$ is an earth-abundant semiconductor with a high optical absorption coefficient in the solar spectrum. Its bandgap can be tuned by controlling the cation sublattice disorder. Thus, it is a potential candidate for photovoltaic absorber materials. However, its important basic properties such as the intrinsic bandgap and effective mass have not yet been quantitatively determined. This paper presents a detailed optical absorption analysis of disordered $ZnSnN_2$ degenerately doped with oxygen ($ZnSnN_{2-x}O_x$) in the ultraviolet to infrared region to determine the conduction-band effective mass (m_c^*) and intrinsic bandgap (E_g). $ZnSnN_{2-x}O_x$ epilayers are *n*-type degenerate semiconductors, which exhibit clear free-electron absorption in the infrared region. By analysing the free-electron absorption using the Drude model, m_c^* was determined to be $(0.37 \pm 0.05)m_0$ (m_0 denotes the free electron mass). The fundamental absorption edge in the visible to ultraviolet region shows a blue shift with increasing electron density. The analysis of the blue shift in the framework of the Burstein-Moss effect gives the E_g value of 0.94 ± 0.02 eV. We believe that the findings of this study will provide important information to establish this material as a photovoltaic absorber.

Photovoltaics represent a promising approach to achieving truly sustainable energy, and considerable efforts have been directed toward the development of high-efficiency photovoltaic cells to meet the increasing global energy demand. In photovoltaic cells based on inorganic semiconductors, the conversion efficiency strongly depends on its bandgap. The theoretical limit of efficiency for a single-junction solar cell reaches a maximum value of ~34%, when the bandgap (E_g) of the semiconductor is ~1.4 eV[1].

Binary semiconductors with an E_g of approximately 1.4 eV are limited to a few compounds such as GaAs, InP, and CdTe[2]. As for semiconductor alloys, $In_xGa_{1-x}N$ is a candidate material for a photovoltaic absorber because the E_g can be tuned to ~1.4 eV by adjusting the indium content (x) to ~0.65[3]. However, these compounds are composed of rare or toxic elements, and it is difficult to produce cost-effective photovoltaic cells based on these semiconductors on large-area substrates. This situation has motivated researchers to seek earth-abundant multi-component semiconductors with an ideal E_g value of 1.4 eV.

In 2013, the first-principles study by Lahourcade *et al.* showed that ternary $ZnSnN_2$ is an earth-abundant semiconductor with an excellent E_g of 1.42 eV[4]. Since then, investigation of $ZnSnN_2$ as a photovoltaic absorber material has been initiated in recent years. However, $ZnSnN_2$ is still not well understood: the synthesis of $ZnSnN_2$ thin film was first reported in 2012[5,6], and the synthesis of $ZnSnN_2$ powders was first reported in 2016[7]. Even the lattice constants have been determined only recently[7,8]. Although extensive study on this material has begun, the basic electronic and optical properties have not been fully elucidated yet.

$ZnSnN_2$ has two phases: ordered-phase and disordered-phase, depending on the cation-sublattice ordering, similar to $ZnGeN_2$. The ordered-phase is derived by alternately replacing the cation-sublattice in the wurtzite structure with Zn and Sn (Fig. 1a). This structure is referred to as β-$NaFeO_2$ structure with orthorhombic symmetry. In the disordered-phase, Zn and Sn randomly occupied the cation-sublattice in the wurtzite-like structure (Fig. 1b). Veal *et al.* conducted the first principle calculations and indicated that the ordered- and disordered-phases have E_g values of 2.3 and 0.98 eV, respectively[9]. Based on these values, we thought that the disordered $ZnSnN_2$ is more ideal for a photovoltaic absorber.

The basic properties of the newly-discovered disordered $ZnSnN_2$ have not yet been thoroughly investigated. For instance, effective mass and the intrinsic E_g of $ZnSnN_2$ remain undetermined. These properties are very

[1]Department of Applied Chemistry, Chubu University, Kasugai, 487-8501, Japan. [2]National Institute for Materials Science (NIMS), Tsukuba, 305-0044, Japan. Correspondence and requests for materials should be addressed to X.C. (email: jscaoxiang@126.com) or N.Y. (email: n-yamada@isc.chubu.ac.jp)

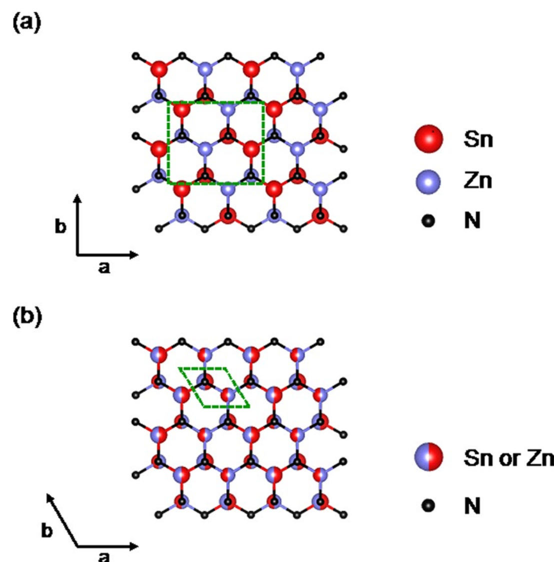

Figure 1. Crystal structures of (**a**) ordered- and (**b**) disordered-phase of $ZnSnN_2$ (from [001] direction). The dotted square in (**a**) and rhombus in (**b**) represent the unit cells. The crystal structure was visualized using VESTA software[51].

E_g [eV]	m_c^*	Ref.
0.98 (Calc.); 1.33–2.38 (Exp.)	$0.12m_0$ (Calc.)	9
1.12 (Calc.); 2.12 (Exp.)	—	10
1.0 (Exp.)	$0.5m_0$ (Exp.)	11
1.64–1.70 (Exp.)	—	12
0.94 ± 0.02 (Calc.)	$(0.37 \pm 0.05)m_0$ (Exp.)	This work

Table 1. Bandgap (E_g) and conduction-band effective mass (m_c^*) of disordered $ZnSnN_2$. 'Exp.' and 'Calc.' represent experimental and calculated values, respectively. (m_0 denotes the free electron mass).

important for establishing $ZnSnN_2$ as a photovoltaic absorber. Insufficient knowledge of the m_c^* and E_g values make it difficult to use this material for photovoltaic absorbers. Although optically determined E_g values have been reported by some research groups, the values are scattered in the range of 1.0–2.0 eV (Table 1)[9–12]. We hypothesize that the reported values are not incorrect and their scattering originates from the blue shift of E_g due to the conduction-band filling effect (the so-called Burstein-Moss shift), because the conduction-electron densities were largely different in each study. As will be described later, this hypothesis was justified, and thus the intrinsic E_g value was successfully determined from the analysis in the framework of the Burstein-Moss effect. As for the reported m_c^* values, a large discrepancy between the theoretical and experimental values exists, which are summarized in Table 1. The theoretical study predicted small m_c^* values of $0.12m_0$ (m_0 denotes the free-electron mass)[9], whereas the experimental study yielded a value four times larger at $0.5m_0$. This large discrepancy motivated us to discover which value is correct. The experimental m_c^* value was derived from the analysis of the Burstein-Moss shift[11]. Strictly speaking, the effective mass determined by this method is not m_c^* but the 'reduced' effective mass (m_{vc}^*), as the m_{vc}^* is a function of m_c^* and the valence-band effective mass (m_v^*), as discussed later. The m_{vc}^* value becomes equal to m_c^* value only when the m_v^* value is much higher than that of m_c^* ($m_c^*/m_v^* \approx 0$). Thus, it is likely that the reported experimental value deviates somewhat from the true value. To obtain the correct m_c^* value, we performed an analysis of the free-electron absorption/reflection in the optical transmittance and reflectance spectra, because the effective mass obtained by this analysis purely corresponds to m_c^*. In fact, m_c^* in many semiconductors has determined by this method.

In addition, it has been reported that $ZnSnN_2$ thin films grown by physical vapor deposition were heavily doped with oxygen ($ZnSnN_{2-x}O_x$), even when oxygen was not intentionally introduced into the growth chamber[4,10,11]. Since the incorporated oxygen acts as an electron donor[5,13], unintentionally oxygen-doped $ZnSnN_2$ films behave as *n*-type degenerate semiconductors with high electrical conductivity and free-electron absorption/reflection in the infrared region. Fioretti *et al.* have addressed the unintentional oxygen-doping problem to obtain nondegenerate $ZnSnN_2$[14]. We can also make use of oxygen-doped $ZnSnN_2$ to determine the conduction-band effective mass by analysing the free-electron absorption/reflection.

In this study, epilayers of disordered $ZnSnN_{2-x}O_x$ with various *x* values were grown. Detailed analysis of their optical absorption/reflection in the ultraviolet to infrared region were performed to reveal the m_c^* and intrinsic E_g values. As a result, the m_c^* and intrinsic E_g values were found to be $(0.37 \pm 0.05)m_0$ and 0.94 ± 0.02 eV, respectively. Herein, we describe the analysis in detail.

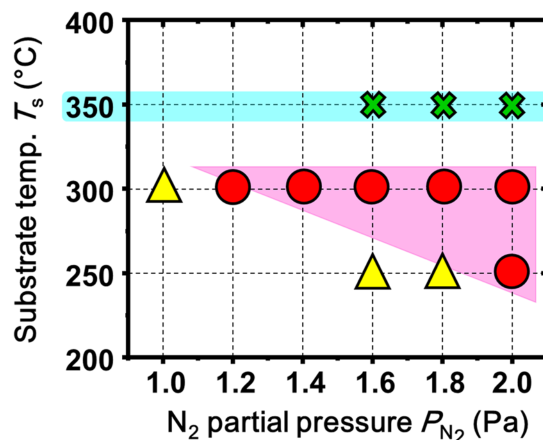

Figure 2. T_s–P_{N_2} growth parameter-based phase diagram of $ZnSnN_2$ films on yttria-stabilized zirconia (111) substrates. The triangles and circles denote polycrystalline and epitaxial films, respectively. Thin films were not grown under the conditions denoted by crosses.

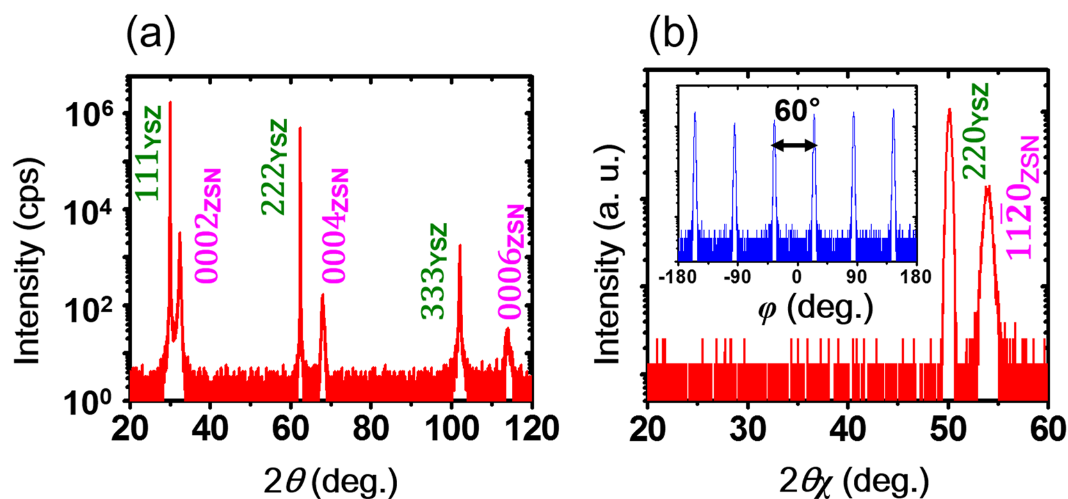

Figure 3. Typical X-ray diffraction patterns scanned in (**a**) θ-2θ and (**b**) φ-$2\theta_\chi$ modes for $ZnSnN_2$ epitaxial films. The inset of part (**b**) represents the φ scan of $ZnSnN_2$ (11$\bar{2}$0) planes. $ZnSnN_2$ is abbreviated to the 'ZSN' in both (**a**) and (**b**).

Results and Discussion

Film Growth and Structure. According to recent literature[15], disordered $ZnSnN_2$ epitaxially grows on (111) yttria-stabilized zirconia (YSZ(111)). Thus, we used YSZ(111) single-crystal substrates for film growth. The structure of the $ZnSnN_2$ film strongly depended on substrate temperatures (T_s) and N_2 partial pressure (P_{N_2}). Figure 2 depicts the phase diagram for $ZnSnN_2$ thin films, as a function of T_s and P_{N_2}. As can be seen in this figure, epitaxial films were obtained in a relatively narrow region (closed circles in the shadowed region).

Figure 3a shows the out-of-plane X-ray diffraction (XRD) pattern of $ZnSnN_2$ epilayers. Although the 111, 222, and 333 diffraction peaks are present in the substrate, only the 0002, 0004, and 0006 diffraction peaks from $ZnSnN_2$ were observed, indicating that the (0001) planes are parallel to the (111) planes of the substrate. The $ZnSnN_2$ epilayers were confirmed to be in the disordered-phase by in-plane φ-scans (see Methods section). Figure 3b shows a typical in-plane XRD pattern (scanned in φ–$2\theta_\chi$ mode) of $ZnSnN_2$ epitaxial layers. The diffraction pattern shows that the (11$\bar{2}$0) planes of the film are aligned with the (110) planes of the substrate. As shown in the inset in Fig. 3b, six evenly spaced 11$\bar{2}$0 peaks were observed in the φ-scan pattern, illustrating the 6-fold rotational symmetry of the basal plane in the disordered-phase (see Fig. 1b). Therefore, it can be confirmed that the disordered $ZnSnN_2$ phase was grown on the YSZ(111) substrate, with the epitaxial relationship of $ZnSnN_2$(0001)//YSZ(111) and $ZnSnN_2$(11$\bar{2}$0)//YSZ(110).

Figure 4a shows the topographic atomic force microscopy (AFM) image of the $ZnSnN_2$ epitaxial film. The image shows that the epitaxial film had a homogeneous compact structure comprising of small grains with lateral diameters of ~300 nm. The surface possessed a rough topography as seen from the three-dimensional image shown in Fig. 4b. The root-mean-square roughness in the 2 × 2 μm^2 area was 1.6 nm. The rough surface is clearly

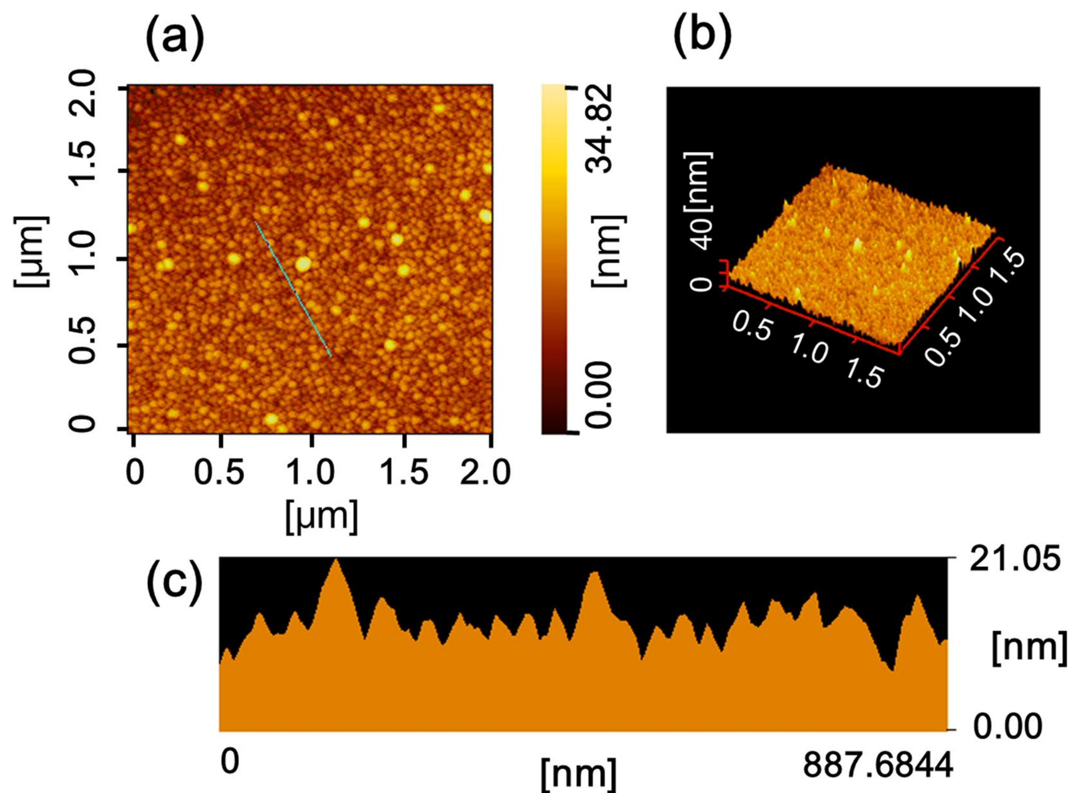

Figure 4. (**a**) Topographic and (**b**) three-dimensional AFM images of the $ZnSnN_2$ epitaxial film surface (2×2 μm^2 scan area), and (**c**) cross-sectional view along the measurement line shown in part (**a**).

illustrated in the cross-sectional image (Fig. 4c). Such rough surface may stem from the resputtering effect[16], which is due to the bombardment of high-energy particles from the plasma. However, the surface roughness did not essentially affect the electrical and optical analyses described below.

Film Composition and Electrical Properties. The cationic composition, hereafter referred to as Zn/(Zn + Sn), was slightly Zn-rich in composition with Zn/(Zn + Sn) of ~0.55, which was almost independent of the growth condition (Fig. 5a). We detected oxygen in all the films, indicating that unintentional oxygen-doping occurred during the film growth ($ZnSnN_{2-x}O_x$). In contrast to Zn/(Zn + Sn), the oxygen concentration, x in $ZnSnN_{2-x}O_x$, depended on P_{N_2} during film growth, as shown in Fig. 5a. The x value decreased with increasing P_{N_2}. The oxygen contamination likely originated from the residual vapor in the growth chamber. The molar ratio of water to nitrogen is expected to decrease as P_{N_2} increases or vice versa. This may be one of the reasons for the x–P_{N_2} dependency.

All the epilayers in the present study showed n-type conductivity. As seen from Fig. 5b, the electron density (n_e) also showed P_{N_2} dependency, as with x. The trend of the n_e–P_{N_2} dependency was very similar to that of the x–P_{N_2}, suggesting that the incorporated oxygen impurities act as electron donors similar to nitrides such as InN[17,18], GaN[19,20], AlN[21,22], and Zn_3N_2[23,24]. Chen *et al*. theoretically predicted that oxygen impurities will occupy the nitrogen sublattice in $ZnSnN_2$ and behave as single electron donors[13]. Since the n_e values were on the order of 10^{20} cm^{-3}, the conduction electrons were highly degenerate (Fig. S1, Supplementary Information).

Effective Mass. Figure 6 shows the optical transmittance (T) and reflectance (R) spectra for the $ZnSnN_{2-x}O_x$ epilayers in the UV to IR region. In this figure, free-electron absorption/reflection can be seen. We performed a fitting analysis of the free-electron absorption/reflection using a dielectric function model to determine the conduction-band effective mass (m_c^*) of disordered $ZnSnN_2$ (see Methods section).

The square and circle marks in Fig. 6a–e represent the experimental data, and the solid lines denote the best fit spectra obtained by the double Tauc-Lorenz (TL) dispersion model coupled with the Drude model. In our combined double TL–Drude model, four fitting parameters for each TL term and two for the Drude term were considered, and described in detail in the Methods section. As can be seen in Fig. 6a–e, the model sufficiently reproduced the spectra across the entire spectral region for all the films. The values of the TL and Drude parameters obtained from the best-fit curves are summarized in Table S1 (Supplementary Information). In addition, we also show the dielectric functions obtained from the fitting analysis in Fig. S2. Using plasma energy (E_p) and n_e values in Table S1, the conduction-band effective mass, m_c^*, can thus be derived (see Methods). The m_c^* values for individual epilayers are plotted in Fig. 7, as a function of n_e. The m_c^* values ranged between

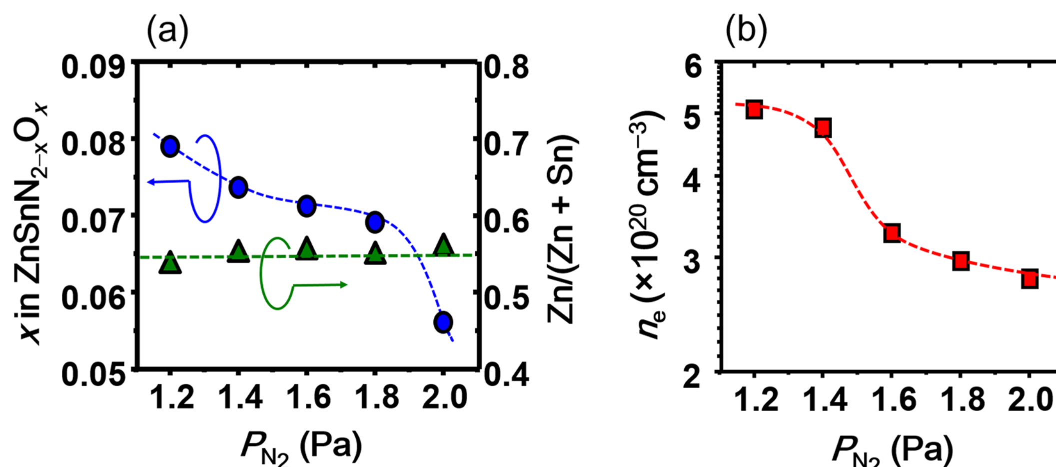

Figure 5. Nitrogen partial pressure (P_{N_2}) dependency of (**a**) oxygen concentration, x in $ZnSnN_{2-x}O_x$, (blue circles), and cation composition, Zn/(Zn + Sn), (green triangles), and (**b**) electron density, n_e, plotted on a logarithmic scale. The dashed lines are visual guides.

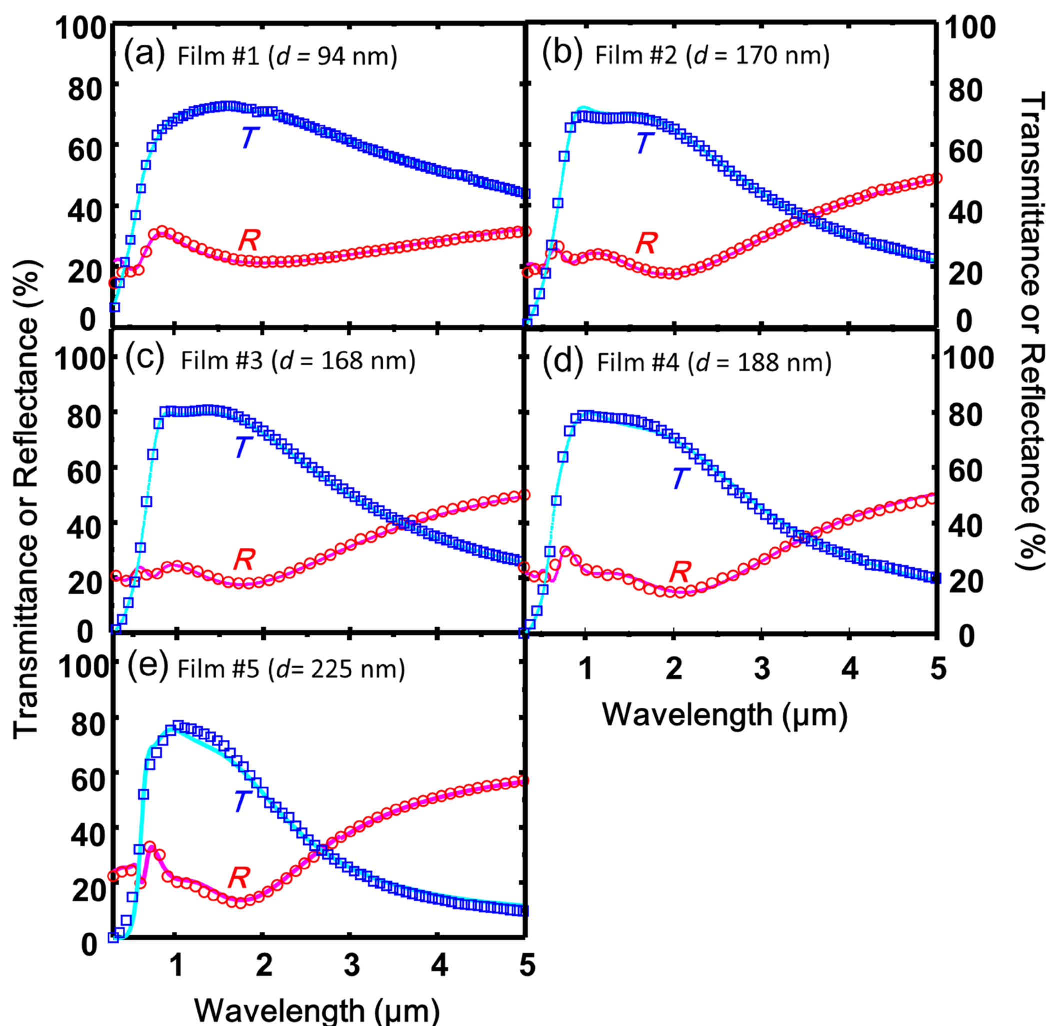

Figure 6. Optical transmittance (labelled by T) and reflectance (labelled by R) spectra for $ZnSnN_{2-x}O_x$ epilayers with different electron densities, n_e: (**a**) $n_e = 2.8 \times 10^{20}\,cm^{-3}$, (**b**) $n_e = 3.0 \times 10^{20}\,cm^{-3}$, (**c**) $n_e = 3.3 \times 10^{20}\,cm^{-3}$ (**d**) $n_e = 4.8 \times 10^{20}\,cm^{-3}$, and (**e**) $n_e = 5.1 \times 10^{20}\,cm^{-3}$. The squares and circles represent the experimental transmittance and reflectance spectra, respectively. The solid lines are the best fit spectra theoretically calculated employing double Tauc-Lorentz dispersion model coupled with the Drude model.

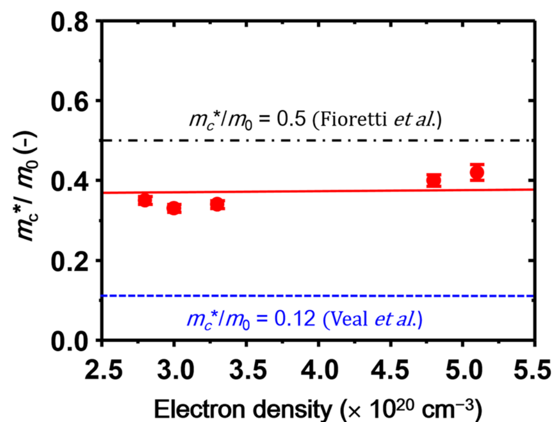

Figure 7. Conduction-band effective mass (m_c^*/m_0) of disordered $ZnSnN_2$ as a function of electron density (red circles). The solid line is a guide for the eyes. The theoretical value reported by Veal *et al.*[9] and experimental value reported by Fioretti *et al.*[11] are shown by the blue dashed line and black dashed-dotted line, respectively.

$(0.32–0.42)m_0$, where m_0 denotes the free electron mass. Therefore, it was concluded that the m_c^* value in disordered $ZnSnN_2$ was $(0.37 \pm 0.05)m_0$.

First principle studies predicted m_c^* values to be as small as ~$0.1m_0$ in both ordered- and disordered $ZnSnN_2$[4,9,25,26]. The predicted m_c^* values are comparable to those in other III–V and Zn-based nitride semiconductors including InN $(0.055m_0)$[27], GaN $(0.2m_0)$[28], GaAs $(0.083m_0)$[29], and Zn_3N_2 $(0.08m_0)$[30]. Although small m_c^* values generally leads to high electron mobility (μ), μ values in the $ZnSnN_2$ epilayers have been reported to be less than or equal to 10 $cm^2 V^{-1} s^{-1}$[9,10]. Indeed, the μ values of the $ZnSnN_2$ epitaxial films in this study were as low as 10–20 $cm^2 V^{-1} s^{-1}$. A recent experimental study by Fioretti *et al.* suggested that the m_c^* value in disordered $ZnSnN_2$ is roughly 4–5 times larger than the predicted values (~$0.5m_0$)[11]. Our results were consistent with their value. Namely, we revealed that the m_c^* values predicted from first-principle calculations are probably underestimated and the m_c^* value is $(0.37 \pm 0.05)m_0$. Therefore, small electron mobility in $ZnSnN_2$ can be partly explained by the somewhat large m_c^*. However, the conduction-band effective mass alone cannot fully account for the low mobility in disordered $ZnSnN_2$. Further investigation of the electron transport properties is still required to understand the reasons for the low electron mobility.

Meanwhile, enhancements in m_c^* with increasing n_e have been reported for various degenerately doped semiconductors such as GaN[31], InN[32], Zn_3N_2[33], GaAs[34], InSb[35], ZnO[36,37], TiO_2[38], and $CdSnO_4$[39]. Such behaviours have been interpreted as a result of the nonparabolic conduction band. In contrast, the m_c^* of $ZnSnN_2$ seems to be almost independent of n_e (Fig. 7), suggesting that the conduction band of disordered $ZnSnN_2$ has a parabolic shape.

Bandgap. The optical absorption coefficients (α) of the $ZnSnN_2$ epilayers were calculated using the relationship $\alpha = d^{-1}\ln[(1-R)/T]$, where d is the thickness of film. Figure 8 shows the absorption coefficient plotted on a log scale as a function of photon energy ($h\nu$) for four $ZnSnN_2$ epilayers with different n_e values. The α spectra showed V-shaped dependency on photon energy. The absorption in the high $h\nu$ region ($h\nu > 1.5$ eV) is due to the fundamental absorption, while the absorption in the low $h\nu$ region (typically $h\nu < 1.2$ eV) corresponds to the free-electron absorption. We defined the optical gap energy (E_g^{opt}) as the photon energy where the extrapolated straight lines of the free-electron absorption and fundamental absorption intersect (see Fig. 8).

The E_g^{opt} varied from 1.25 to 1.51 eV as n_e increased from 2.8×10^{20} to 5.1×10^{20} cm^{-3}. Therefore, the increase in n_e caused a blue shift of the E_g^{opt}. The blue shift has frequently been observed in degenerate $ZnSnN_2$ and is interpreted as the Burstein-Moss (BM) shift, which is a consequence of the conduction band filling effect due to heavy oxygen-doping[4,9–11]. For degenerate *n*-type semiconductors, n_e-dependent E_g^{opt} due to the BM effect is expressed as

$$E_g^{opt} = E_g + \Delta E_g^{BM} = E_g + \frac{\hbar^2}{2m_{vc}^*}(3\pi^2 n_e)^{2/3} \tag{1}$$

where E_g is the intrinsic bandgap energy and m_{vc}^* is the reduced effective mass given by $m_{vc}^* = (1/m_v^* + 1/m_c^*)^{-1}$ (m_v^* denotes the valence-band effective mass). In heavily doped semiconductors, bandgap narrowing due to electron–electron and electron–impurity interactions also occurs: the bandgap narrowing partially compensates the bandgap widening due to the BM shift[40–42]. We calculated the bandgap narrowing due to electron–electron and electron–impurity interactions ($\Delta E_g^{e,e}$ and $\Delta E_g^{e,i}$, respectively) in a manner similar to the procedure described in literature[43]. Both the $\Delta E_g^{e,e}$ and $\Delta E_g^{e,i}$ were quite small in comparison with ΔE_g^{BM}, and those exhibited roughly linear dependence on $n_e^{2/3}$. Consequently, the total bandgap shift, $\Delta E_g = \Delta E_g^{BM} - \Delta E_g^{e,e} - \Delta E_g^{e,i}$, was almost proportional to $n_e^{2/3}$ (see Fig. S3, Supplementary Information). This result justifies plotting E_g^{opt} as a function of $n_e^{2/3}$ to derive the intrinsic bandgap, E_g. The E_g^{opt} values for all films are plotted (closed circles) together with the values reported in literature for disordered $ZnSnN_2$ films (squares[11] and triangles[9]) as a function of $n_e^{2/3}$ in Fig. 9.

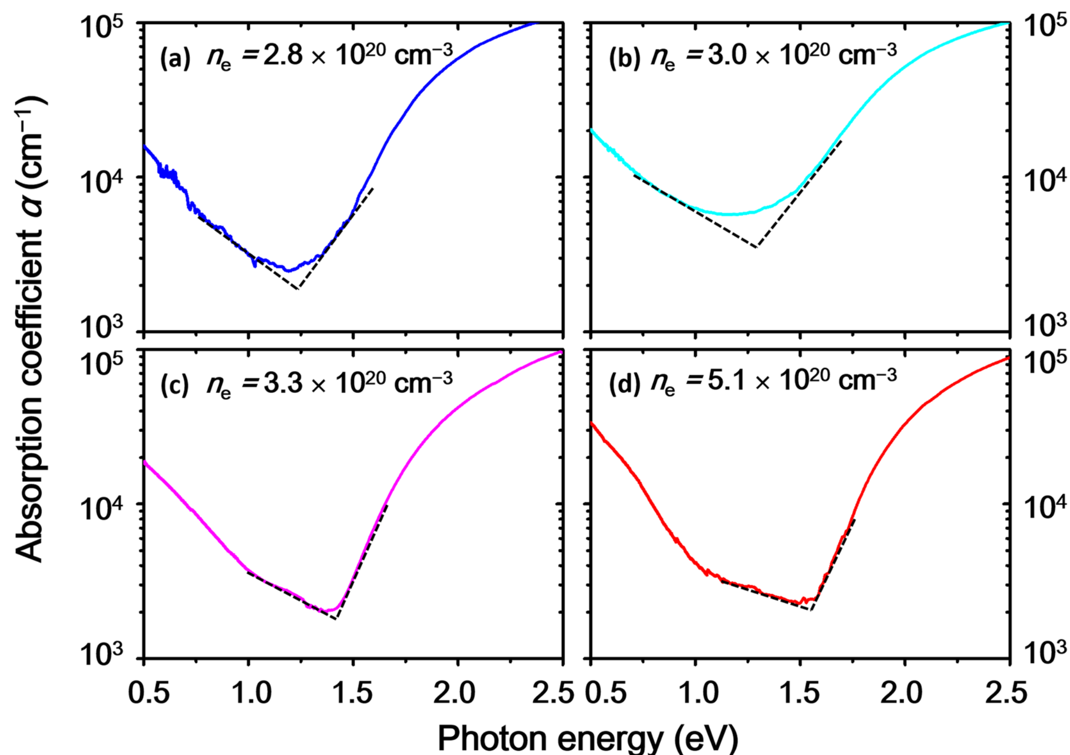

Figure 8. Absorption coefficient (α) as functions of photon energy for four selected $ZnSnN_2$ films with different electron densities, n_e. The photon energy at which extrapolated straight dashed lines intersect corresponds to the optical bandgap energy (E_g^{opt}).

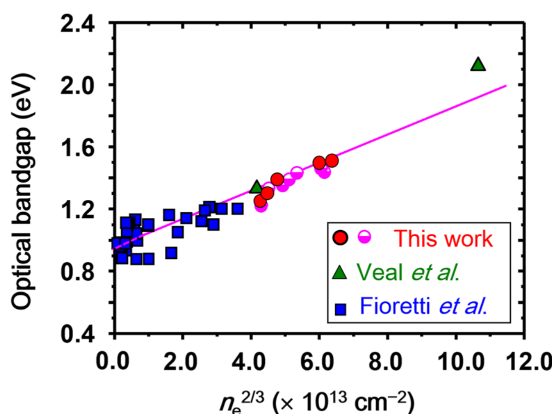

Figure 9. Optical bandgap of disordered $ZnSnN_2$ films as a function of electron density to the power of 2/3, $n_e^{2/3}$. The circles denote the data obtained in the present study (closed circles for films in Table S1 and open circles for additional films). Data obtained from Fioretti *et al.*[11] and Veal *et al.*[9] are denoted as squares and triangles, respectively.

Moreover, additional $ZnSnN_2$ epilayers were grown under conditions similar to the films presented in Table S1. The E_g^{opt} values of these additional films are also presented in Fig. 9 (open circles). As seen from Fig. 9, E_g^{opt} shows linear dependency on $n_e^{2/3}$, which is consistent with the trend shown in Fig. S3. It is striking that the E_g values in this study correlate with the values reported in literature. Hence, a linear regression fit (least-square approach) was applied to all the data including the values reported in literature (Fig. 9), indicating universality within the used data, the intercept of the straight-line gives the intrinsic bandgap (E_g). Accordingly, the E_g value of disordered $ZnSnN_2$ was determined to be 0.94 ± 0.02 eV. The E_g value reasonably agrees with the value predicted by the first-principle study for fully disordered $ZnSnN_2$ ($E_g = 0.98$ eV)[9].

In the present study, we did not take the cation composition into account for the determination of E_g. The cation composition may be relevant for the E_g value, though it is not clear whether the effect is significant or not. The cation composition dependency of E_g is currently a research focus for $ZnSnN_2$.

Conclusion

In summary, the conduction-band effective mass and intrinsic bandgap of disordered $ZnSnN_2$ were optically determined to get an insight into the fundamental properties. Heavily oxygen-doped $ZnSnN_{2-x}O_x$ epitaxial layers were grown with various electron densities. These epilayers exhibited free-electron absorption/reflection in the infrared region. The detailed analysis of the free-electron absorption/reflection revealed that the conduction-band effective mass is $(0.37 \pm 0.05)m_0$. To the best of our knowledge, this study is the first to quantitatively determine m_c^*. Furthermore, the blue shift of the optical bandgap was analysed in the framework of the Burstein-Moss effect to determine the intrinsic bandgap, which has been in debate to date. Our optical bandgap values and those obtained from literature showed a universal 2/3-power dependency on the electron density. From this dependency, the intrinsic bandgap of disordered $ZnSnN_2$ was determined to be 0.94 ± 0.02 eV. We believe that the findings in the present study provide important information to establish this material as a photovoltaic absorber.

Methods

Thin Film Growth. $ZnSnN_2$ thin films were epitaxially grown on YSZ(111) single-crystalline substrates by reactive radio-frequency (RF) magnetron sputtering using a $Zn_{0.5}Sn_{0.5}$ alloy target (diameter of 10 cm and purity of 3 N), at T_s ranging from 250 to 350 °C. The base pressure of ~2×10^{-4} Pa was established prior to the film-growth. An RF power of 70 W was applied to the target. A mixture of Ar and N_2 gas with various $N_2/(N_2 + Ar) \equiv f(N_2)$ ratios was introduced into the chamber through two independent mass flow controllers with a total flow rate of 5 sccm. The working pressure in the chamber (P_w) was held at 2.0 Pa during film growth. Films were grown under P_{N_2} ranging from 1.0 to 2.0 Pa. The nitrogen partial pressure was defined as $P_{N_2} = f(N_2) \times P_w$. The growth time was adjusted to obtain films with thicknesses of 100–300 nm.

Characterization Methods. A Rigaku ATX-G X-ray diffractometer with Cu Kα radiation was employed to perform out-of-plane (θ-2θ) and in-plane (φ-2θ_χ) scans to evaluate the structure of the films. To ensure that grown $ZnSnN_2$ epilayers were in the disordered-phase, we performed in-plane φ-scans. Provided that the $ZnSnN_2$ films are in ordered-phase with the orthorhombic symmetry, a characteristic 110 peak will be observed at an in-plane diffraction angle ($2\theta_\chi$) of 20.07° in the φ-scans (Fig. S4a in Supplementary Information). We carried out the in-plane φ-scans at the fixed $2\theta_\chi$ angle of 20.07° several times, but no peak was observed (Fig. S4b in Supplementary Information). Even when the $2\theta_\chi$ angle was slightly increased or decreased, the 110 peak did not appear. These results indicate that the $ZnSnN_2$ films epitaxially grown on YSZ(111) were in the disordered-phase, which is consistent with the results reported in literature[15]. The surface morphology was characterized with an atomic force microscope (Hitachi AFM5100N). The compositions (Zn/(Zn + Sn) and x) of the $ZnSnN_2$ films were examined by X-ray photoelectron spectroscopy (PHI Versa Probe), using monochromated Al Kα ($h\nu = 1486.6$ eV) radiation. The relative sensitivity factor (RSF) approach was exploited to determine the compositions. It was confirmed that the compositions determined by the RSF method were consistent with those determined by Rutherford backscattering spectrometry[33,44]. Hence, it was concluded that the compositions in this study are sufficiently reliable. The description of the RSF approach are detailed in the Supplementary Information. Electrical properties were determined by Hall-effect measurements in the van der Pauw configuration (Toyo Corp. Resitest 8200). Optical transmittance and reflectance were collected between 0.3 and 5.0 µm using a UV-Vis-NIR spectrophotometer (Shimadzu UV-3150) and FTIR spectrometer (Shimadzu IRAffinity-1).

Fitting Analysis of *T* and *R* Spectra. Owing to the large electron density on the order of 10^{20} cm^{-3}, free-electron absorption and reflection are clearly seen in the infrared region (see Fig. 6a–e). The well-known Drude dielectric model was employed to describe the optical response by the free electrons in the IR region. The Drude function is given by,

$$\varepsilon_D(E) = -\frac{E_P^2}{E^2 - i\Gamma_D E} \tag{2}$$

where E is the photon energy, Γ_D represents the broadening parameter, and E_P denotes the plasma energy, which can be expressed as

$$E_P = \hbar\left(\frac{e^2 \cdot n_e}{\varepsilon_0 \cdot m_c^*}\right)^{\frac{1}{2}} \tag{3}$$

Here, $\hbar$, e, and ε_0, denote the reduced Planck constant, elemental charge, and the static dielectric constant of free space, respectively. As seen from Equation 3, E_p^2 is theoretically proportional to n_e when the dielectric response in the IR region can be described by the Drude model. In fact, E_p^2 showed a linear dependency on n_e (Fig. S5, Supplementary Information), suggesting appropriate use of the Drude function.

In addition to the Drude model, the Tauc-Lorentz (TL) dispersion model was considered to describe the optical response across the whole spectral region (see Fig. 6). The explicit expression of the TL model is given in literature[45]. The TL model has proved to be useful for the description of the fundamental absorption of many semiconductors[36,45–47]. Recently, Deng *et al.* demonstrated that the dielectric response of $ZnSnN_2$ in UV to visible region can be reproduced by double TL functions[48]. Hence, we modelled the dielectric function of degenerate $ZnSnN_2$ as a sum of double TL ($\varepsilon_{TL1}(\omega)$ and $\varepsilon_{TL2}(\omega)$) and Drude functions, whereby $\varepsilon(\omega) = \varepsilon_{TL1}(\omega) + \varepsilon_{TL2}(\omega) + \varepsilon_D(\omega)$. In this study, $\varepsilon_{TL1}(\omega)$ and $\varepsilon_{TL2}(\omega)$ were assigned to the fundamental absorption of the bandgap and the transition that corresponds to the M_4–M_3 transition in group-III nitrides, respectively[49,50]. Theoretical T and R spectra calculated via the Fresnel formulas combined with the $\varepsilon(\omega)$ function were fitted to the experimental spectra. In the

fitting procedure, a set of {A_{TL}, Γ_{TL}, E_0, E_T} for each TL term and {E_p, Γ_p} for the Drude term were selected as fitting parameters. Here, A_{TL}, Γ_{TL}, E_0, and E_T in the TL term represent the oscillator strength, broadening parameter, resonance energy, and Tauc gap energy, respectively[45].

References

1. Shockley, W. & Queisser, H. J. Detailed balance limit of efficiency of *p-n* junction solar cells. *J. Appl. Phys.* **32**, 510–519 (1961).
2. Polman, A., Knight, M. W., Garnett, E. C., Ehrler, B. & Sinke, W. C. Photovoltaic materials: Present efficiencies and future challenges. *Science* **352**, aad4424 (2016).
3. Zhang, X. B. *et al.* Simulation of $In_{0.65}Ga_{0.35}N$ single-junction solar cell. *J. Phys. D: Appl. Phys.* **40**, 7335–7338 (2007).
4. Lahourcade, L. *et al.* Structural and optoelectronic characterization of RF sputtered $ZnSnN_2$. *Adv. Mater.* **25**, 2562–2566 (2013).
5. Coronel, N. C., Lahourcade, L., Delaney, K. T., Shing, A. M. & Atwater, H. A. Earth-abundant $ZnSn_xGe_{1-x}N_2$ alloys as potential photovoltaic absorber materials. *Proc. of the 38th IEEE Photovoltaic Specialists Conference*, 003204–003207, https://doi.org/10.1109/PVSC.2012.6318259 (2012).
6. Feldberg, N. *et al.* $ZnSnN_2$: A new earth-abundant element semiconductor for solar cells. *Proc. of the 38th IEEE Photovoltaic Specialists Conference*, 002524—002527, https://doi.org/10.1109/PVSC.2012.6318108 (2012).
7. Kawamura, F., Yamada, N., Imai, M. & Taniguchi, T. Synthesis of $ZnSnN_2$ crystals via a high-pressure metathesis reaction. *Cryst. Res. Technol.* **51**, 220–224 (2016).
8. Quayle, P. C., He, K., Shan, J. & Kash, K. Synthesis, lattice structure, and band gap of $ZnSnN_2$. *MRS Commun.* **3**, 135–138 (2013).
9. Veal, T. D. *et al.* Band gap dependence on cation disorder in $ZnSnN_2$ solar absorber. *Adv. Energy Mater.* **5**, 1501462 (2015).
10. Feldberg, N. *et al.* Growth, disorder, and physical properties of $ZnSnN_2$. *Appl. Phys. Lett.* **103**, 042109 (2013).
11. Fioretti, A. N. *et al.* Combinatorial insights into doping control and transport properties of zinc tin nitride. *J. Mater. Chem. C* **3**, 11017–11028 (2015).
12. Qin, R. F. *et al.* Semiconducting $ZnSnN_2$ thin films for Si/$ZnSnN_2$ *p-n* junctions. *Appl. Phys. Lett.* **108**, 142104 (2016).
13. Chen, S., Narang, P., Atwater, H. A. & Wang, L. W. Phase stability and defect physics of a ternary $ZnSnN_2$ semiconductor: first principles insights. *Adv. Mater.* **26**, 311–315 (2014).
14. Fioretti, A. N. *et al.* Solar cells: effects of hydrogen on acceptor activation in ternary nitride semiconductors. *Adv. Electron. Mater.* **3**, 1600544 (2017).
15. Senabulya, N. *et al.* Stabilization of orthorhombic phase in single-crystal $ZnSnN_2$ films. *AIP Adv.* **6**, 075019 (2016).
16. Jones, R. E., Standley, C. L. & Maissel, L. I. Re-emission coefficients of Si and SiO_2 films deposited through rf and dc sputtering. *J. Appl. Phys.* **38**, 4656–4662 (1967).
17. Duan, X. M. & Stampfl, C. Defect complexes and cluster doping of InN: First-principles investigations. *Phys. Rev. B* **79**, 035207 (2009).
18. Wu, J. *et al.* Effects of electron concentration on the optical absorption edge of InN. *Appl. Phys. Lett.* **84**, 2805–2807 (2004).
19. Götz, W. *et al.* Activation energies of Si donors in GaN. *Appl. Phys. Lett.* **68**, 3144–3146 (1996).
20. Wright, A. F. Substitutional and interstitial oxygen in wurtzite GaN. *J. Appl. Phys.* **98**, 103531 (2005).
21. Mattila, T. & Nieminen, R. M. *Ab initio* study of oxygen point defects in GaAs, GaN, and AlN. *Phys. Rev. B* **54**, 16676 (1996).
22. Slack, G. A., Schowalter, L. J., Morelli, D. & Freitas, J. A. Jr. Some effects of oxygen impurities on AlN and GaN. *J. Crystal Growth* **246**, 287–298 (2002).
23. Long, R., Dai, Y., Yu, L., Guo, M. & Huang, B. B. Structural, electronic, and optical properties of oxygen defects in Zn_3N_2. *J. Phys. Chem. B* **113**, 3379–3383 (2007).
24. Cao, X., Sato, A., Ninomiya, Y. & Yamada, N. Oxygen-doped zinc nitride as a high-mobility nitride-based semiconductor. *J. Phys. Chem. C* **119**, 5327–5333 (2015).
25. Paudel, T. R. & Lambrecht, W. R. L. First-principles study of phonons and related ground-state properties and spectra in Zn-IV-N_2 compounds. *Phys. Rev. B* **78**, 115204 (2008).
26. Punya, A., Lambrecht, W. R. L. & Van Schilfgaarde, M. Quasiparticle band structure of Zn-IV-N_2 compounds. *Phys. Rev. B* **84**, 165204 (2011).
27. Millot, M. *et al.* Determination of effective mass in InN by high-field oscillatory magnetoabsorption spectroscopy. *Phys. Rev. B* **83**, 125204 (2011).
28. Drechsler, M. *et al.* Determination of the conduction band electron effective mass in hexagonal GaN. *Jpn. J. Appl. Phys.* **34**, L1178 (1995).
29. Cardona, M. Electron effective masses of InAs and GaAs as a function of temperature and doping. *Phys. Rev.* **121**, 752–758 (1961).
30. Cao, X., Ninomiya, Y. & Yamada, N. Zinc nitride as a potential high-mobility transparent conductor. *Phys. Status Solidi A* **214**, 1600472 (2017).
31. Skierbiszewski, C. *et al.* Large, nitrogen-induced increase of the electron effective mass in $In_yGa_{1-y}N_xAs_{1-x}$. *Appl. Phys. Lett.* **76**, 2409–2411 (2000).
32. Foley, C. P. & Tansley, T. L. Pseudopotential band structure of indium nitride. *Phys. Rev. B* **33**, 1430–1433 (1986).
33. Cao, X., Yamaguchi, Y., Ninomiya, Y. & Yamada, N. Comparative study of electron transport mechanisms in epitaxial and polycrystalline zinc nitride films. *J. Appl. Phys.* **119**, 025104 (2016).
34. Szmyd, D. M., Porro, P., Majerfeld, A. & Lagomarsino, S. Heavily doped GaAs:Se. I. Photoluminescence determination of the electron effective mass. *J. Appl. Phys.* **68**, 2367–2375 (1990).
35. Spitzer, W. G. & Fan, H. Y. Determination of optical constants and carrier effective mass of semiconductors. *Phys. Rev.* **106**, 882–890 (1957).
36. Fujiwara, H. & Kondo, M. Effects of carrier concentration on the dielectric function of ZnO:Ga and In_2O_3:Sn studied by spectroscopic ellipsometry: Analysis of free-carrier and band-edge absorption. *Phys. Rev. B* **71**, 075109 (2005).
37. Minami, T., Sato, H., Ohashi, K., Tomofuji, T. & Takata, S. Conduction mechanism of highly conductive and transparent zinc oxide thin films prepared by magnetron sputtering. *J. Cryst. Growth* **117**, 370–374 (1992).
38. Furubayashi, Y. *et al.* Transport properties of *d*-electron-based transparent conducting oxide: Anatase $Ti_{1-x}Nb_xO_2$. *J. Appl. Phys.* **101**, 093705 (2007).
39. Wu, X., Coutts, T. J. & Mulligan, W. P. Properties of transparent conducting oxides formed from CdO and ZnO alloyed with SnO_2 and In_2O_3. *J. Vac. Sci. Technol. A* **15**, 1057–1062 (1997).
40. Berggren, K. F. & Sernelius, B. E. Band-gap narrowing in heavily doped many-valley semiconductors. *Phys. Rev. B* **24**, 1971–1986 (1981).
41. Hamberg, I., Granqvist, C. G., Berggren, K. F., Sernelius, B. E. & Engström, L. Band-gap widening in heavily Sn-doped In_2O_3. *Phys. Rev. B* **30**, 3240–3249 (1984).
42. Jain, S. C., McGregor, J. M. & Roulston, D. J. Band-gap narrowing in novel III-V semiconductors. *J. Appl. Phys.* **68**, 3747–3749 (1990).
43. Feneberg, M. *et al.* Many-electron effects on the dielectric function of cubic In_2O_3: Effective electron mass, band nonparabolicity, band gap renormalization, and Burstein-Moss shift. *Phys. Rev. B* **93**, 045203 (2016).
44. Núñez, C. G. *et al.* On the zinc nitride properties and the unintentional incorporation of oxygen. *Thin Solid Films* **520**, 1924–1929 (2012).

45. Jellison, G. E. Jr. & Modine, F. A. Parameterization of the optical functions of amorphous materials in the interband region. *Appl. Phys. Lett.* **69**, 371–373 (1996).
46. Kamiya, T., Nomura, K. & Hosono, H. Electronic structure of the amorphous oxide semiconductor a-$InGaZnO_{4-x}$: Tauc-Lorentz optical model and origins of subgap states. *Phys. Status Solidi A* **206**, 860–867 (2009).
47. Jost, P. *et al.* Disorder-induced localization in crystalline pseudo-binary GeTe–Sb_2Te_3 alloys between $Ge_3Sb_2Te_6$ and GeTe. *Adv. Funct. Mater.* **25**, 6399–6406 (2015).
48. Deng, F. *et al.* Determination of the basic optical parameters of $ZnSnN_2$. *Opt. Lett.* **40**, 1282–1285 (2015).
49. Djurišić, A. B. & Li, E. H. Modeling the optical constants of hexagonal GaN, InN, and AlN. *J. Appl. Phys.* **85**, 2848–2853 (1999).
50. Djurišić, A. B. & Li, E. H. Dielectric function models for describing the optical properties of hexagonal GaN. *J. Appl. Phys.* **89**, 273–282 (2001).
51. Momma, K. & Izumi, F. VESTA 3 for three-dimensional visualization of crystal, volumetric and morphology data. *J. Appl. Crystallogr.* **44**, 1272–1276 (2011).

Acknowledgements

This work was supported by Japan Society for the Promotion of Science (JSPS) KAKENHI (Grant number 16H04500). We also thank Masunori Kawamura of Chubu University for providing support of instrument operation.

Author Contributions

N.Y. and F.K. designed the experiments. X.C. performed fabrication and measurements. T.T., Y.N. and N.Y. were the PIs. X.C. and N.Y. wrote the manuscript. All authors discussed the results and reviewed the manuscript.

Additional Information

Supplementary information accompanies this paper at https://doi.org/10.1038/s41598-017-14850-7.

Competing Interests: The authors declare that they have no competing interests.

Publisher's note: Springer Nature remains neutral with regard to jurisdictional claims in published maps and institutional affiliations.

Open Access This article is licensed under a Creative Commons Attribution 4.0 International License, which permits use, sharing, adaptation, distribution and reproduction in any medium or format, as long as you give appropriate credit to the original author(s) and the source, provide a link to the Creative Commons license, and indicate if changes were made. The images or other third party material in this article are included in the article's Creative Commons license, unless indicated otherwise in a credit line to the material. If material is not included in the article's Creative Commons license and your intended use is not permitted by statutory regulation or exceeds the permitted use, you will need to obtain permission directly from the copyright holder. To view a copy of this license, visit http://creativecommons.org/licenses/by/4.0/.

© The Author(s) 2017